

Ab Initio Simulations of Temperature Dependent Phase Stability and Martensitic Transitions in NiTi

Justin B. Haskins,^{†,§} Alexander E. Thompson,^{‡,§} and John W. Lawson*,¶

¹ *AMA Inc., Thermal Materials Protection Branch, NASA Ames Research Center, Moffett Field, California 94035, USA, USRA, Thermal Materials Protection Branch, NASA Ames Research Center, Moffett Field, California 94035, USA, and Thermal Materials Protection Branch, NASA Ames Research Center, Moffett Field, California 94035, USA*

E-mail: john.w.lawson@nasa.gov

*To whom correspondence should be addressed

†AMA Inc., Thermal Materials Protection Branch, NASA Ames Research Center, Moffett Field, California 94035, USA

‡USRA, Thermal Materials Protection Branch, NASA Ames Research Center, Moffett Field, California 94035, USA

¶Thermal Materials Protection Branch, NASA Ames Research Center, Moffett Field, California 94035, USA

§Contributed equally to this work

2

Abstract

3 For NiTi based alloys, the shape memory effect is governed by a transition from a
4 low-temperature martensite phase to a high-temperature austenite phase. Despite con-
5 siderable experimental and computational work, basic questions regarding the stability
6 of the phases and the martensitic phase transition remain unclear even for the simple
7 case of binary, equiatomic NiTi. We perform *ab initio* molecular dynamics simulations
8 to describe the temperature-dependent behavior of NiTi and resolve several of these
9 outstanding issues. Structural correlation functions and finite temperature phonon
10 spectra are evaluated to determine phase stability. In particular, we show that finite
11 temperature, entropic effects stabilize the experimentally observed martensite (B19')
12 and austenite (B2) phases while destabilizing the theoretically predicted (B33) phase.
13 Free energy computations based on *ab initio* thermodynamic integration confirm these
14 results and permit estimates of the transition temperature between the phases. In
15 addition to the martensitic phase transition, we predict a new transition between the
16 B33 and B19' phases. The role of defects in suppressing these phase transformations is
17 discussed.

18 Shape memory alloys are materials that after deformation recover their original shape
19 upon heating. They are technologically important for a wide range of applications, including
20 actuators, shape-morphing wings and next generation space suits, among others. Nickel
21 Titanium (nitinol) is perhaps the best-known example in this class of alloys and figures
22 prominently in many commercial applications. The shape memory effect in NiTi is driven
23 by a martensitic phase transition from a low temperature martensite phase (B19') to a high
24 temperature austenite phase (B2).^{1,2} Many applications involving shape memory alloys are
25 tied to the specific value of the martensitic phase transition temperature.³ Having the ability
26 to tune this transition temperature, for example, through ternary additions in NiTi-based
27 alloys,^{3–5} will open the door to significantly more far-reaching applications. However, even
28 for binary, equiatomic NiTi, which is the simplest example in this class of materials, basic
29 questions regarding the stability of the phases and the martensitic phase transition remain
30 unclear. In this paper, we resolve several of these important, outstanding issues.

31 Experimentally, the high temperature austenite phase of NiTi has the cubic B2 ($Pm\bar{3}m$
32 symmetry) structure. The low temperature martensite phase has the monoclinic B19'
33 ($P2_1/m$ symmetry) structure, with an experimentally determined angle γ of 98° .^{6,7} The
34 transition temperature between the two phases is reported to be approximately 341 K.⁸ Rel-
35 evant crystal structures are shown in Figure 1. Considerable computational work has been
36 performed to understand the phases of NiTi and related materials. In particular, density
37 functional theory (DFT) studies^{9–22} have provided many insights into the energetics and
38 properties of NiTi; but they have also generated new unanswered questions. For example,
39 DFT formation energies for B2 are in good agreement with experiments;^{23–26} however, B2 is
40 predicted to be dynamically unstable at $T = 0$, i.e. certain phonons modes have imaginary
41 frequencies.²⁷ Recent attempts using small systems to include finite temperatures effects into
42 B2 stability analyses have given contradictory results.^{28,29} On the other hand, B19' at the ex-
43 perimental monoclinic angle γ of 98° is dynamically stable at $T = 0$; however, the computed
44 structure is unstable to shear.¹² Huang *et al.* determined the DFT ground state of NiTi

45 at $T = 0$ to be a new orthorhombic phase (B33) with an angle of $\gamma = 107.3^\circ$.³⁰ However,
46 the B33 structure has not been observed experimentally in NiTi and its crystal symmetry
47 ($Cmcm$) is incompatible with the shape memory effect, and therefore cannot represent the
48 martensitic phase of this material. Thus, after considerable computational analysis, we are
49 in the unsatisfying position that the two experimentally observed phases for NiTi have un-
50 determined stability; whereas the only computed stable phase has never been observed and
51 is incompatible with the shape memory effect.

52 To address these discrepancies, we perform high accuracy, *ab initio* molecular dynamics
53 (AIMD) simulations based on density functional theory combined with extended thermody-
54 namic integration methods to evaluate the stability and relative free energies for the defect-
55 free, single crystal phases (B2, B19', B33) of NiTi for a range of temperatures up to 900 K.
56 These materials are strongly anharmonic, and therefore, methods based primarily on phonon
57 analysis, even at finite temperatures, will not capture the full behavior. This necessitates
58 high accuracy computations of the free energy. We show that finite temperature, entropic
59 effects resolve many of the controversies derived from previous studies, bringing computa-
60 tion into much closer agreement with experiment. Specifically, we show that entropic effects
61 stabilize both B2 and B19' while destabilizing B33. Furthermore, the martensitic transition
62 temperature is estimated between these stable phases. In addition, we also identify a new
63 phase transition between B33 and B19'.

64 For B2, B19', and B33, we consider phase stability from several complementary view-
65 points. For each case, the lattice vectors of the AIMD simulation cells are optimized such
66 that all finite temperature components of the stress tensor are zero. This procedure not only
67 accounts for thermal expansion, but also places the system at a critical point on the free
68 energy surface. Next, we examine deviations of the crystalline structure from ideality during
69 the course of the simulations in these optimized cells. Structural evolution is evaluated quan-
70 titatively with: (1) normalized position correlation functions (NPCFs)³¹ and (2) atomic dis-
71 placement scatter diagrams.³² The NPCF is proportional to $\sum_i \langle (r_i(t-t_0) - R_i^0) \cdot (r_i(t_0) - R_i^0) \rangle$

72 where $r_i(t)$ are the atomic trajectories from the AIMD simulation, R_i^0 is the ideal reference
73 lattice vectors of interest and the brackets are ensemble averages. For long times ($t \rightarrow \infty$),
74 vibrational motion becomes uncorrelated, and therefore, $\text{NPCF} \rightarrow 0$ indicates stabilization
75 with respect to the reference lattice whereas nonzero values indicate the converse. We plot
76 the atomic displacements explicitly relative to the reference structures on scatter diagrams.
77 Significant deviations from zero displacement signal an instability.

78 Both NPCFs as well as atomic displacement scatter plots are shown in Figure 2 for
79 144 atom cells of B33, B19', and B2. Large cell sizes are required to eliminate finite size
80 effects (see Supplemental Documentation for extensive convergence tests for all computed
81 properties). Figure 2a, b, and c, shows very different behavior for the three phase at different
82 temperatures. For B33, the NPCFs indicate structural stability at lower temperatures, 50 K
83 and 300 K, but instability for $T > 300$ K. Convergence times at 300 K are almost two
84 orders of magnitude larger than at 50 K. This may indicate the proximity of a stability
85 transition for B33. Interestingly, the B19' phase loses its $T = 0$ non-zero shear stress even
86 at low T and maintains its ideal configuration across the full 50 to 600 K temperature range
87 considered. Perhaps most striking is that while the B2 structure is unstable at 50 K, it
88 stabilizes for $T > 300$ K. Unlike B33, the NPCF convergence rates for B2 increase with
89 increasing temperature.

90 The atomic displacements scatter plots for B2, B19', and B33 are shown in the overlay
91 plots in Figure 2a, b, and c, respectively. For each case, displacements are provided for
92 50 K (blue circles) and 600 K (red squares). At low temperatures, B33 displacements are
93 negligible; however, at high temperatures, large displacements on the order of 0.5 Å can
94 be seen in the a direction. Displacements in a result from thermally induced motion along
95 the [100](011) stacking fault, which previously has been shown from DFT calculations to
96 be important for the martensitic transition.^{9,10} At low and high temperatures, the B19'
97 phase exhibits only minor displacements, ~ 0.05 Å. The B19' displacements do not show
98 any particular ordering and can most likely be attributed to vibrational motion, as indicated

99 by the loss of correlation in the NPCF. The B2 phase at low temperatures shows large
100 displacements $\sim 0.4 \text{ \AA}$ from ideality. At higher temperatures, however, these displacements
101 largely vanish, as seen in the tight clustering near the origin. Both the NPCF and the atomic
102 scatter plots indicate that for $T > 300 \text{ K}$, the high temperature phase of NiTi is very closely
103 approximated by ideal B2.

104 Phase stability is further investigated by explicit computation of temperature-dependent
105 phonons as derived from the AIMD simulations.^{33,34} Imaginary phonon modes (represented
106 as negative numbers) indicate the crystal structure is dynamically unstable, i.e. it is not a
107 local minima of the energy. Phonon spectra are shown in Figure 3 at both zero-temperature
108 and at 600 K. It is important to note that these results are very sensitive to cell size, and
109 therefore, using sufficiently large cells is crucial to obtain reliable results. Because of this,
110 144 atom cells were employed for computations on all phases (see Supplemental Figures S3-
111 S8 for convergence study results). The B33 phase, given in Figure 3a, develops imaginary
112 modes at 600 K through the lowering of the TA mode along the $\Gamma \rightarrow A$ direction. Phonon
113 dispersions for the B19' phase shows stability across the full temperature range investigated,
114 as shown in Figure 3b. Most dramatically perhaps, the imaginary modes reported for the
115 B2 $T = 0 \text{ K}$ phonon dispersion lift and become positive at 300 K, as shown in Figure 3a,
116 indicating stabilization of this phase, consistent with the structure analysis of Figure 2.

117 The stress tensor, structure, and phonon analyses provide a complementary picture of
118 the temperature dependent stability of the three phases that is consistent with experiment.
119 Namely, stable phases at a given temperature exhibit the following properties: all compo-
120 nents of the stress tensor (normal stresses and shears) are on average zero; the NPCF goes
121 to zero in finite time; and all phonon modes are positive. Our results therefore show that
122 finite temperature, entropic effects stabilize the high-temperature B2 phase between 50 and
123 300 K. Similarly, the low-temperature B33 phase is progressively destabilized, fully losing
124 stability between 300 K and 600 K. The B19' phase, on the other hand, is unstable to shear
125 at $T = 0$ but exhibits full stability from 50 K up to 700 K.

126 To obtain further insights into phase stability as well as transitions between the phases,
127 we next compute the relative free energies of the phases. Vibrational entropy is frequently
128 evaluated via the quasi-harmonic approximation (QHA). However, stability issues at $T = 0$
129 invalidates this approach for B2 due to the appearance of imaginary phonon modes. Alter-
130 natively, stable, finite temperature phonon spectra can be used with the QHA expressions
131 to obtain entropy estimates. However, for strongly anharmonic materials such as NiTi, this
132 approach will not be a good approximation to the full anharmonic entropy. This strong
133 anharmonicity therefore necessitates the use of high accuracy methods for computing free
134 energies. For this reason, we use two different methods based on thermodynamic integration
135 to compute the free energies. The computations should be exact to within the accuracy of
136 DFT.

137 Our first approach is a generalization of the stress-strain methods developed previously
138 for transition metals.³⁵ Those methods based on Bain path integration are necessarily vol-
139 ume conserving; however, many systems of interest including NiTi do not conserve volume
140 between the phases. We generalized that approach to account for arbitrary volume changes
141 in an exact way. We expect this method to have applicability beyond what is presented
142 here. Our generalized stress-strain method requires a well defined, continuous path in lattice
143 vector space between the two given phases. For NiTi, the monoclinic angle, γ , provides a
144 natural, continuous parameter to connect the three phases of interest shown in Figure 1.
145 In general, multiple paths can be considered; however, the B33 \rightarrow B19' \rightarrow B2 path was deter-
146 mined to be the best behaved and is equivalent to motion along the $\langle 100 \rangle \{110\}$ generalized
147 stacking faults. Spontaneous motion along this fault was found in the high temperature B33
148 phase during structural stability tests. The B33 \rightarrow B19' path is largely a transformation in γ -
149 space, as the lattice vectors are of comparable magnitude, while the B19' \rightarrow B2 path involves
150 non-trivial changes to both γ as well as the lattice vectors. Optimization of the simulation
151 cells to obtain zero stress is required to ensure the obtained free energy differences, which
152 are Helmholtz free energy differences, are equivalent to Gibbs free energy differences. We

153 find the internal atomic coordinates for the 144 atom cell for this path to transform contin-
154 uously and that the stresses converge rapidly (< 10 ps) (see Supplemental Figure S9). It
155 should be noted that while free energy differences between stable phases can be rigorously
156 computed, evaluation of free energies differences involving unstable structures is still an area
157 of active investigation. Therefore, free energies involving unstable structures may contain
158 some systematic error as discussed recently.³⁶

159 Our second approach uses the Einstein crystal method to compute free energy differences
160 at isolated points along the transformation paths. These computations were used to check the
161 stress-strain method and were only performed at free energy mimima along the transformation
162 path. The reference harmonic free energy is obtained from the force constants associated
163 with the temperature dependent phonon dispersions. This approach overcomes difficulties
164 in using $T = 0$ K phonon dispersions with imaginary modes. For each stable crystal at a
165 given temperature, thermodynamic integration is performed from the system described by
166 the harmonic reference potential to the one described by DFT. The integration can result in
167 anharmonic contributions to the free energy on the order of 5 meV/atom compared to the
168 harmonic reference free energy. This nontrivial anharmonic contribution to the free energy
169 can shift the transition temperature by as much as 100 K and thus confirms the need for
170 high accuracy or exact methods to study these systems.

171 Free energy results using the generalized stress-strain method at 0, 50, 300, and 600 K
172 are given in Figure 4a as a function of γ . Einstein crystal results are shown as open symbols
173 for validation. Agreement between the methods is excellent (≤ 1 meV/atom). The $T = 0$
174 curve reproduces previous DFT results, and clearly shows that B2 and B19' are not energetic
175 minima whereas B33 is a stable minimum, as reported by Huang *et al.*³⁰ We see however
176 that the free energy surface changes considerably as a function of temperature. Between
177 B33 and B19', a small but distinguishable barrier develops between the phases for $T =$
178 $50K - 300K$. Above 600 K, however, the free energy is monotonically decreasing from B33
179 to B19'. Importantly, B19' develops a clearly defined free energy minima above 50 K. Thus,

180 B19' is entropically stabilized and develops into a separate phase distinct from B33. The
181 B2 phase is unstable to transitions to B19' until 300 K, above which a free energy barrier
182 develops stabilizing this phase as a local minima. These results are consistent with the
183 structural and phonon analysis.

184 Further detail is provided by Figure 4b where free energy differences relative to the most
185 stable phase are mapped as a function of T and γ . Blue and red represent small and large
186 free energy differences, respectively. The free energies are again derived from the generalized
187 stress-strain method. The free energy map illustrates the stability regions associated with
188 each of the phases: B33, B19', and B2. White circles indicate stable points of each phase,
189 i.e. all finite temperature stresses are zero and all finite temperature phonons are real and
190 positive. Thus each white circle represents a stable, free energy minimum for that phase and
191 the white lines denote the extent of the stable free energy basins. Free energy and stability
192 results are provided for 50 K as well as between 0 and 900 K in steps of 100 K. The regions
193 of stability for each phase are found to be $0 < T < 300$ K for B33, $50 < T < 600$ K for B19',
194 and $T > 300$ K for B2. Interestingly, the B19' angle is shown to be a function of temperature,
195 ranging from $\sim 100^\circ$ at 50 K to $\sim 98^\circ$ at 600 K. Furthermore, the stable basin of B19' is
196 relatively shallow suggesting that γ values for this phase might be fairly sensitive to small
197 changes in stress. This could be important since stress fields associated with defects could
198 potentially alter the value of γ quoted here. The free energy results allow us to estimate the
199 phase transition temperatures. In particular from Figure 4, the transition between B33 and
200 B19' appears to occur between 50 and 300 K. The B19' \rightarrow B2 free energy path, is uphill until
201 600 K, indicating that a transition occurs between 300 and 600 K.

202 Differences in the Gibb's free energy (ΔG) between the various stable phases as a function
203 of T are plotted in Figure 5. Vanishing of the free energy difference indicates a phase
204 transition. For ΔG between B33 and B19', a new phase transition is predicted to occurs
205 at 75 ± 26 K. For B19' to B2, ΔG goes to zero at 500 ± 14 K. The larger error for the low-
206 T transition is a function of the slope of ΔG and the target accuracy of 1 meV/atom.

207 The low values for the B33→B19' transition temperature explains the lack of experimental
208 evidence for B33, despite being energetically favored at 0 K. If B33 becomes unstable at
209 low temperatures, it may be difficult to synthesize and therefore to observe. The B19'→B2
210 transition temperature is roughly 150 K above the experimental value of 341 K.⁸ However,
211 the methods used to obtain this value, based on *ab initio* thermodynamic integration, are
212 numerically exact to within the accuracy of DFT. Therefore, we expect it to be a reliable
213 estimate of the martensitic transition temperature for defect-free, single crystal NiTi. The
214 non-trivial difference with experimental values is most likely due to defects that have been
215 shown to suppress transition temperatures in this and related materials.³⁷ This also suggests
216 that improved processing resulting in higher material quality could produce materials with
217 higher measured transition temperatures. In addition, it is also known that the transition
218 temperature is dependent on the heating and cooling rates with slower rates giving higher
219 transition temperatures. Since we use equilibrium methods to estimate this temperature,
220 our results correspond effectively to infinitely slow rates. For that reason, we expect them
221 to be an upper bound for the experimental transition temperature.

222 We have performed a comprehensive computational analysis based on *ab initio* molecular
223 dynamics of the stability and transitions between the major phases of NiTi: B2, B19', and
224 B33. Considerable previous computational analysis based mainly on $T = 0$ DFT resulted
225 in significant discrepancies between experiment and computation. We have shown that by
226 including temperature dependent entropic effects into the computations, many of these dif-
227 ferences can be resolved. We show that B2 and B19' are stabilized due to these entropic
228 effects whereas B33 is destabilized. These materials are shown to be highly anharmonic. An-
229 harmonic contributions to the free energy can shift the transition temperature by as much
230 as 100K and thus necessitates the need for high accuracy or exact methods to study these
231 systems. We develop an generalized stress-strain method to perform such computations. The
232 phase transition temperature between B2 and B19' is estimated to be approximately 500 K
233 for defect-free, single crystals which is about 150 K above experimental results. Defects and

234 non-equilibrium rate effects are expected to suppress the transition temperature and bring
235 it more into line with experiments.³⁷ This also suggests opportunities to obtain higher tran-
236 sition temperatures with current materials by improved material processing. A new phase
237 transition in this material is identified between B19' and B33 with an estimated temperature
238 of 75 K. High temperature destabilization of B33 and the corresponding low transition tem-
239 perature to B19' could explain why B33 has not yet been observed experimentally. Defects
240 could affect this transition as well.

241 Methods

242 Simulations are performed with the Vienna *Ab Initio* Simulation Package (VASP)^{38–41} using
243 the frozen core all-electron projector augmented wave (PAW) method^{42,43} and the generalized
244 gradient approximation of Perdew, Burke, and Ernzerhof.⁴⁴ All DFT-MD simulations employ
245 an energy cutoff of 269.5 eV, an electronic energy convergence criteria of 1×10^{-7} eV, a time
246 step of 3.0 fs, and \sim 3000 k-points per inverse atom. Furthermore, electronic smearing is
247 handled through the Methfessel-Paxton scheme⁴⁵ with a smearing width of 0.05 eV, and
248 the computations are not spin polarized. For both Ni and Ti the 3d and 4s electrons are
249 included in the valence. This valence configuration was found to produce free energy results
250 within 1 meV/atom agreement with smaller core simulations that include the 3p in the the
251 Ti valence. Computations are performed on 144 atom supercells, which were found to be
252 free of vibrational size effects. Temperature is controlled through the use of a Langevin
253 thermostat with a simulation-time equivalent friction factor of 100 fs.

254 For the B33, B19', and B2 phases, structures were optimized at temperature (from 50 to
255 900 K) to provide negligible stress. Optimization is carried out by performing 3 ps AIMD
256 simulations, obtaining stresses averaged over this period, and altering the cell to decrease the
257 stress. This procedure was iterated until all stresses were < 1 kbar. During the optimization,
258 the value of γ for B19' and B33 was allowed to change to produce negligible shear stress, γ was

held 90° for B2. The value of γ was sensitive to temperature for B19', while it remained near 107.32° for B33. Barrierless, and spontaneous, B33→B19' and B19'→B2 phase transitions were found upon optimization at critical temperatures of 400 K and 800 K, respectively. At and above the critical temperature, geometry optimization was performed with γ for B33 and B19' being held to the terminal values of 107.32° and 97°, respectively.

Zero-temperature phonon dispersions were obtained from the frozen phonon approach using displacements of 0.01 Å. Temperature dependent phonons were computed by fitting force data from 50 ps DFT-MD simulations to a force constant matrix.^{33,34} The force constant matrix was then symmetrized in accordance with the crystal structure. Imaginary frequencies were indicated with negative numbers.

Helmholtz free energy computations were provided by a generalized stress-strain method and through a modified Einstein crystal approach. The generalized stress-strain method involves the incremental interpolation of lattice vectors and atomic positions between stress optimized B33 and B19' structures as well as between stress optimized B19' and B2 structures. The resulting path is effectively γ -dependent. The transition between the phases is represented by changes in the tensor composed of the cell lattice vectors, $\Omega(\lambda)$, where λ is a mixing parameter that describes a linear change between the initial and final lattice vectors. The initial and final structures correspond to λ values of 0 and 1, respectively, and AIMD simulations were performed on structures at nine intermediate values of λ . The Helmholtz free energy difference between the initial and final structures was then obtained by

$$\Delta F = \int_0^1 V_\lambda \left[(\sigma \Omega^{-T}) : \frac{\partial \Omega}{\partial \lambda} \right] d\lambda, \quad (1)$$

where σ is the stress tensor and V_λ is the λ -dependent volume. Derivation and validation of this expression is presented in the supplementary material. Extensive convergence tests were performed with respect to simulation parameters and system size (see Supplementary Fig. S10) to ensure accurate measures of free energy.

283 Checks of the generalized stress strain approach were conducted using the Einstein crystal
284 approach for structures representing free energy minima. The temperature-dependent force
285 constant matrix was employed as a reference harmonic state for which the free energy was
286 known. Thermodynamic integration was then performed between the force constant reference
287 and DFT to provide the anharmonic contribution to free energy. The free energy difference
288 between the reference potential and DFT is given by $\Delta F = \int_0^1 \langle \frac{\partial U}{\partial \lambda} \rangle_\lambda d\lambda$. In this expression
289 $U = U^H - \lambda(U^H - U^{DFT})$, where U^H is the harmonic reference potential energy and U^{DFT}
290 represent the DFT potential energy. The mixing parameter, λ , defines a linear change
291 between the harmonic potential and DFT. MD simulations are performed for potential energy
292 surfaces resulting from λ values of 0, 0.25, 0.5, 0.75, and 1 to produce a smoothly varying
293 $\partial U / \partial \lambda$. Convergence tests (see Supplementary Figs. S11 and S12) were performed to ensure
294 accurate measures of free energy.

295 Acknowledgement

296 This work was supported by funding from the NASA Aeronautics Research Mission Direc-
297 torate's Transformational Tools & Technologies (TTT) project. We benefited from discus-
298 sions with Charles Bauschlicher, Ronald Noebe, and Othmane Benafan.

299 References

- 300 (1) Shaw, J. A.; Kyriakides, S. Thermomechanical Aspects of NiTi. *J. Mech. Phys. Solids*
301 **1995**, *43*, 1243–1281.
- 302 (2) Benafan, O.; Padula, S. A.; Noebe, R. D.; Sisneros, T.; Vaidyanathan, R. Role of B19'
303 martensite deformation in stabilizing two-way shape memory behavior in NiTi. *J. Appl.*
304 *Phys.* **2012**, *112*, 093510.
- 305 (3) Ma, J.; Karaman, I.; Noebe, R. D. High Temperature Shape Memory Alloys. *Int. Mater.*
306 *Rev.* **2013**, *55*, 257–315.

307 (4) Zarnetta, R.; Takahashi, R.; Young, M. L.; Savan, A.; Furuya, Y.; Thienhaus, S.; Maaß,;
308 Rahim, M.; Frenzel, J.; Brunken, H. et al. Identification of Quaternary Shape Memory
309 Alloys with Near-Zero Thermal Hysteresis and Unprecedented Functional Stability.
310 *Adv. Funct. Mater.* **2010**, *20*, 1917–1923.

311 (5) Bucsek, A. N.; Hudish, G. A.; Bigelow, G. S.; Noebe, R. D.; Stebner, A. P. Composition,
312 compatibility, and the functional performances of Ternary NiTiX high-temperature
313 shape memory alloys. *Shap. Mem. Superelasticity* **2016**, *2*, 62.

314 (6) Michal, G. M.; Sinclair, R. The Structure of TiNi Martensite. *Acta Crystallogr. B* **1981**,
315 *37*, 1803–1807.

316 (7) Brüher, W.; Gotthardt, R.; Kulik, A.; Mercier, O.; Staub, F. Powder Neutron Diffrac-
317 tion Study of Nickel-Titanium Martensite. *J. Phys. F.* **1983**, *13*, L77–L81.

318 (8) Prokishkin, S. D. On the Lattice Parameters of Phases in Binary Ti-Ni Shape Memory
319 Alloys. *Acta Mater.* **2004**, *52*, 4479–4492.

320 (9) Hatcher, N.; Kontsevoi, O. Y.; Freeman, A. J. Martensitic Transformation Path in NiTi.
321 *Phys. Rev. B* **2009**, *79*, 020202.

322 (10) Hatcher, N.; Kontsevoi, O. Y.; Freeman, A. J. Role of Elastic and Shear Stabilities in
323 the Martensitic Transformation Path of NiTi. *Phys. Rev. B* **2009**, *80*, 144203.

324 (11) Vishnu, G.; Strachan, A. Size Effects in NiTi from Density Functional Theory Calcu-
325 lations. *Phys. Rev. B* **2012**, *85*, 014114.

326 (12) Wagner, M. F.-X.; Windl, W. Lattice Stability, Elastic Constants and Macroscopic
327 Moduli of NiTi Martensites from First Principles. *Acta Mater.* **2008**, *56*, 6232–6245.

328 (13) Wang, J.; Sehitoglu, H. Resolving Quandaries Surrounding NiTi. *Appl. Phys. Lett.*
329 **2012**, *101*, 081907.

330 (14) Huang, X.; Bungaro, C.; Godlevsky, V.; Rabe, K. M. Lattice Instabilities of Cubic NiTi
331 from First Principles. *Phys. Rev. B* **2001**, *65*, 014108.

332 (15) Holec, D.; Friák, M.; Dlouhý, A.; Neugebauer, J. *Ab initio* Study of Pressure Stabilized
333 NiTi Allotropes: Pressure-Induced Transformations and Hysteresis Loops. *Phys. Rev.*
334 *B* **2011**, *84*, 224119.

335 (16) Kibey, S.; Sehitoglu, H.; Johnson, D. Energy Landscape for Martensitic Phase Trans-
336 formation in Shape Memory NiTi. *Acta Mater.* **2009**, *57*, 1624–1629.

337 (17) Šesták, P.; Černý, M.; Pokluda, J. On the Effect of Deformation Twins on Stability of
338 B19' Structure in NiTi Martensite. *Comput. Mater. Sci.* **2014**, *87*, 107–111.

339 (18) Pasturel, A.; Colinet, C.; Manh, D.; Paxton, A.; van Schilfgaarde, M. Electronic Struc-
340 ture and Phase Stability Study in the Ni-Ti System. *Phys. Rev. B* **1995**, *52*, 15176–
341 15190.

342 (19) Wang, X.-Q. Twinned Structure for Shape Memory: First-Principles Calculations.
343 *Phys. Rev. B* **2008**, *78*, 092103.

344 (20) Ye, Y.; Chan, C.; Ho, K. Structural and Electronic Properties of the Martensitic Alloys
345 TiNi, TiPd, and TiPt. *Phys. Rev. B* **1997**, *56*, 3678–3689.

346 (21) Zeng, Z.-Y.; Hu, C.-E.; Cai, L.-C.; Chen, X.-R.; Jing, F.-Q. Molecular Dynamics Study
347 of the Melting Curve of NiTi Alloy under Pressure. *J. Appl. Phys.* **2011**, *109*, 043503.

348 (22) Šesták, P.; Černý, M.; Pokluda, J. Can Twinning Stabilize B19' Structure in NiTi
349 Martensite? *Intermetallics* **2011**, *19*, 1567–1572.

350 (23) Hu, R.; Nash, P.; Chen, Q. Enthalpy and Formation of the Al-Ni-Ti System. *J. Phase*
351 *Equilibria Diffus.* **2009**, *30*, 559–563.

352 (24) Kubaschewski, O. The Heats of Formation in the System Aluminum + Nickel + Tita-
353 nium. *Trans. Faraday Soc. Engl.* **1958**, *54*, 814–820.

354 (25) Gachon, J.; Notin, M.; Hertz, J. The Enthalphy of Mixing of the Intermediate Phases
355 in the Systems FeTi, CoTi, and NiTi by Direct Reaction Calorimetry. *Thermochim.*
356 *Acta* **1981**, *48*, 155–164.

357 (26) Guo, Q.; Kleppa, O. Standard Enthalpies of Formation of Some Alloys Formed between
358 Group IV Elements and Group VIII Elements, Determined by High-Temperature Direct
359 Synthesis Calorimetry: II. Alloys of (Ti, Zr, Hf) with (Co, Ni). *J. Alloys Compd.* **1998**,
360 *269*, 181–186.

361 (27) Parlinski, K.; Parlinska-Wojtan, M. Lattice Dynamics of NiTi Austenite, Martensite,
362 and R Phase. *Phys. Rev. B* **2002**, *66*, 064307.

363 (28) Sourvatzis, P.; Legut, D.; Eriksson, O.; Katsnelson, M. Ab Initio Study of Interacting
364 Lattice Vibrations and Stabilization of the Beta Phase in Ni-Ti Shape-Memory Alloys.
365 *Phys. Rev. B* **2010**, *81*, 092201.

366 (29) Zarkevich, N. A.; Johnson, D. D. Stable Atomic Structure of NiTi Austenite. *Phys.*
367 *Rev. B* **2014**, *90*, 060102.

368 (30) Huang, X.; Ackland, G. J.; Rabe, K. M. Crystal Structures and Shape-Memory Behav-
369 ior of NiTi. *Nature Mater.* **2003**, *2*, 307–311.

370 (31) Vocadlo, L.; Alf  , D.; Gillan, M.; Wood, I.; Brodholt, J.; David Price, G. Possible
371 Thermal and Chemical Stabilization of Body-Centered-Cubic Iron in the Earth's Core.
372 *Nature* **2003**, *31*, 536.

373 (32) Asker, C.; Belonoshko, A.; Mikhaylushkin, A.; Abrikosov, I. First-Principles Solution
374 to the Problem of Mo Lattice Stability. *Phys. Rev. B* **2008**, *77*, 220102(R).

375 (33) Hellman, O.; Abriksosov, I. A.; Simak, S. I. Lattice Dynamics of Anharmonic Solids
376 from First Principles. *Phys. Rev. B* **2011**, *84*, 180301.

377 (34) Hellman, O.; Abriksosov, I. A.; Simak, S. I. Temperature Dependent Effective Potential
378 Method for Accurate Free Energy Calculations of Solids. *Phys. Rev. B* **2013**, *87*, 104111.

379 (35) Carzola, C.; Alf  , D.; Gillan, M. J. Constraints on the Phase Diagram of Molybdenum
380 from First-Principles Free-Energy Calculations. *Phys. Rev. B* **2012**, *85*, 064113.

381 (36) van de Walle, A.; Hong, Q.; Kadkhodaei, S.; Sun, R. The free energy of mechanically
382 unstable phases. *Nat. Commun.* **2015**, *6*, 7559.

383 (37) Tehrani, A.; Shahrokhshahi, H.; Parvin, N.; Brgoch, J. Influencing the Martensitic
384 Phase Transition in NiTi Through Point Defects. *J. Appl. Phys.* **2015**, *118*, 014901.

385 (38) Kresse, G.; Hafner, J. *Ab Initio* Molecular Dynamics for Liquid Metals. *Phys. Rev. B*
386 **1993**, *47*, 558.

387 (39) Kresse, G.; Hafner, J. *Ab Initio* Molecular-Dynamics Simulation of the Liquid-Metal-
388 Amorphous-Semiconductor Transition in Germanium. *Phys. Rev. B* **1994**, *49*, 14251.

389 (40) Kresse, G.; Furthm  ller, J. Efficiency of *Ab Initio* Total Energy Calculations for Metals
390 and Semiconductors Using a Plane-Wave Basis Set. *Comput. Mat. Sci.* **1996**, *6*, 15.

391 (41) Kresse, G.; Furthm  ller, J. Efficient Iterative Schemes for *Ab Initio* Total Energy Cal-
392 culations Using a Plane-Wave Basis Set. *Phys. Rev. B* **1996**, *54*, 11169.

393 (42) Blochl, P. E. Projector Augmented-Wave Method. *Phys. Rev. B* **1994**, *50*, 17953.

394 (43) Kresse, G.; Joubert, D. From Ultrasoft Pseudopotentials to the Projector Augmented-
395 Wave Method. *Phys. Rev. B* **1999**, *59*, 1758.

396 (44) Perdew, J. P.; Burke, K.; Ernzerhof, M. Generalized Gradient Approximation Made
397 Simple. *Phys. Rev. Lett.* **1996**, *77*, 3865.

398 (45) Methfessel, M.; Paxton, A. T. High-precision sampling for brillouin-zone integration in
399 metals. *Phys. Rev. Lett.* **1997**, *78*, 1396.

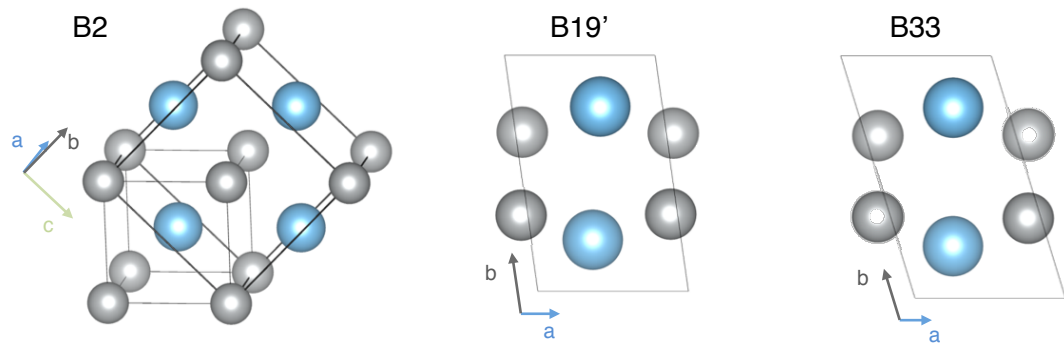


Figure 1: Phases of NiTi including B2 in its primitive, 2 atom cell as well as in a four atom cell that is analogous to the primitive cells of B19' and B33. The monoclinic angle, γ , is defined to be between the a and b lattice vectors.

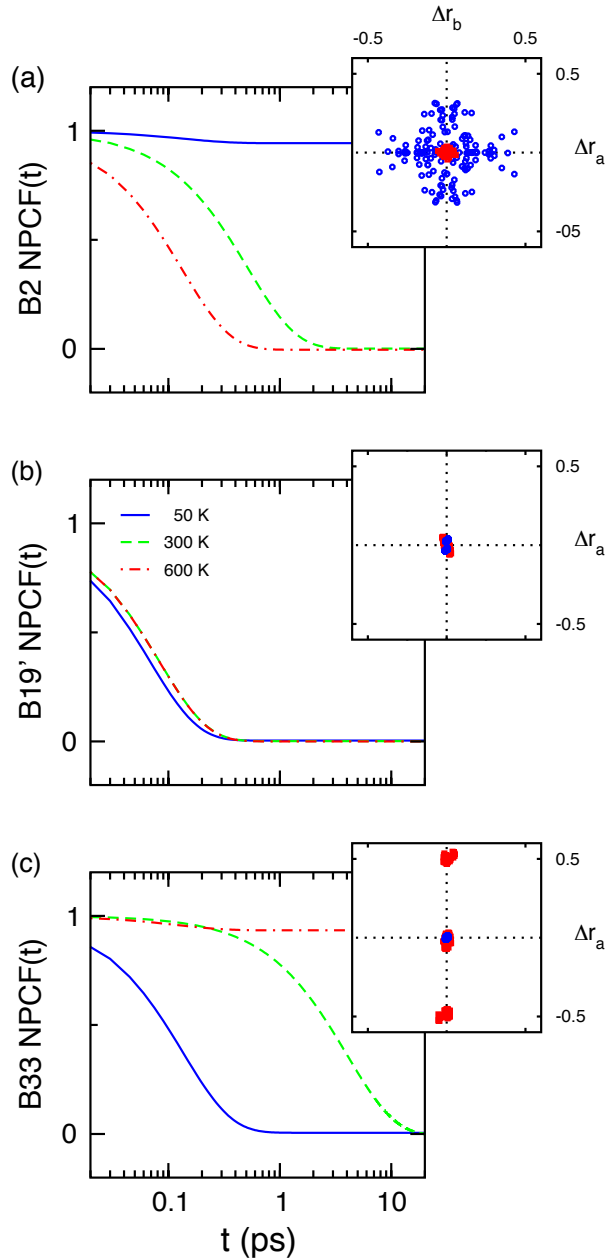


Figure 2: Normalized position correlation function (NPCF) and scatter plots of average atomic displacements from ideal positions along the a (Δr_a) and b (Δr_b) lattice vectors for (a) B2, (b) B19', and (c) B33. The NPCFs are given for the 144 supercell at 50, 300, and 600 K and differentiate between stable ($\text{NPCF}(\infty) \sim 0$) and unstable ($\text{NPCF}(\infty) \sim 1$) structures. For all cells, scatter plots are given for the lowest tested temperature of 50 K (blue circles) and 600 K (red squares).

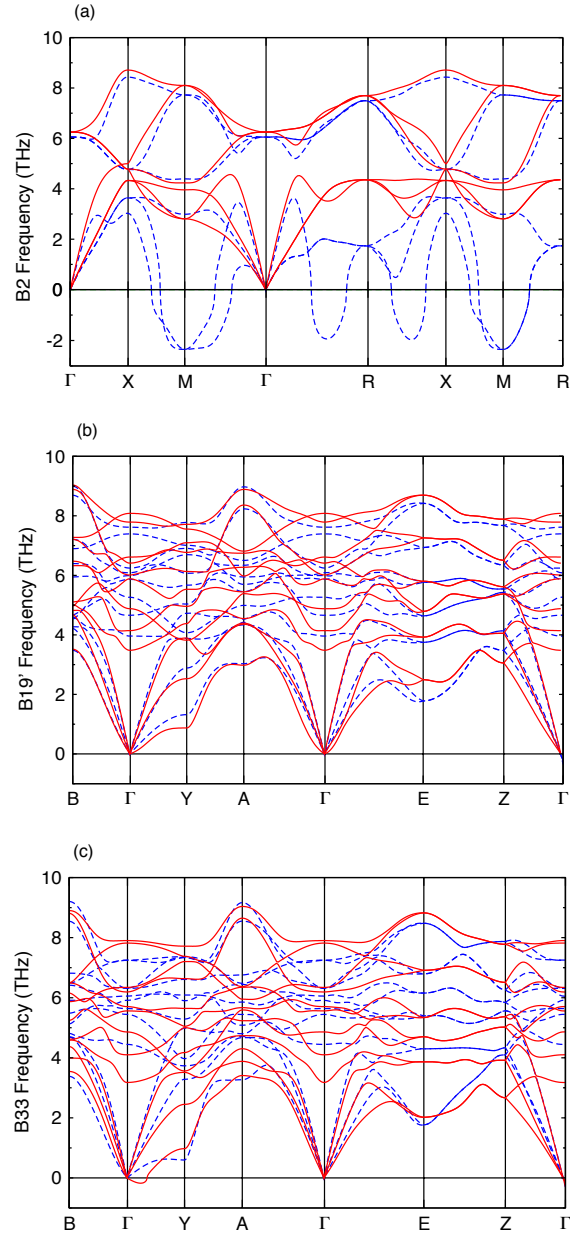


Figure 3: Phonons of the (a) B2, (b) B19', and (c) B33 phases of NiTi at 0 K (blue, dashed line) and 600 K (red, solid line). Temperature-dependent phonons are extracted from simulations using the 144 atom supercell.

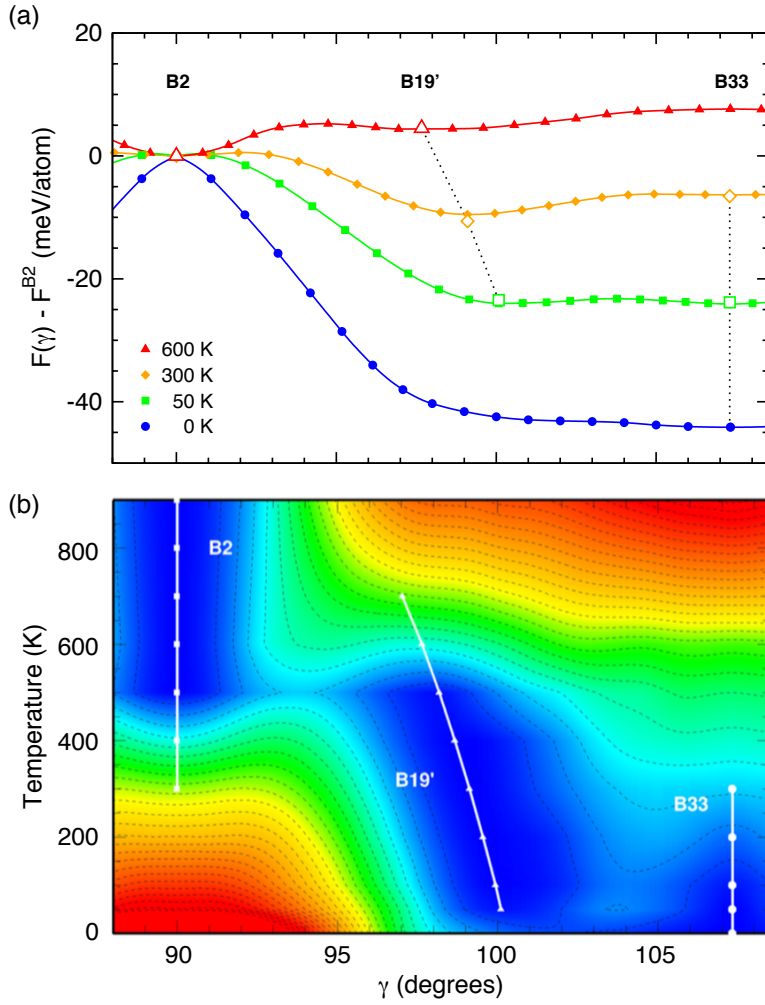


Figure 4: Helmholtz free energy along the γ reaction coordinate as a function of temperature. (a) The free energy profile along the γ reaction coordinate for 0, 50, 300, and 600 K. Filled symbols and lines are obtained through the generalized stress-strain method, while open symbols are provided for free energy minima using the Einstein crystal approach. Error bars for the Einstein crystal method are < 1 meV/atom and not visible at the present scale. (b) Free energy color map as a function of temperature and γ . Regions of low free energy are given as blue, while regions of high free energy are given as red. White lines describe stability basins and also indicates the temperature dependence for the B19' monoclinic angle.

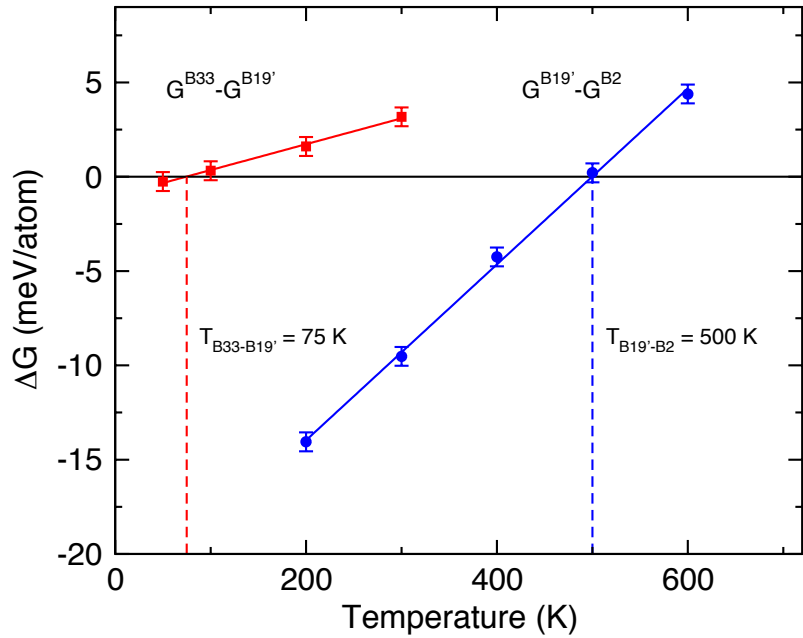


Figure 5: Gibbs free energy differences between B33 and B19' (squares) as well as between B19' and B2 (circles) phases as a function of temperature. Interpolated transition temperatures are indicated with dashed lines. Error bars reflect the 1 meV/atom accuracy of the computations.

SUPPLEMENTAL MATERIAL

CONTENTS

1. Energy and Structure	2
2. Finite Temperature Optimization	4
3. Phonon Dispersions	6
4. Free Energy: Generalized Stress-Strain Method	8
5. Free Energy: Einstein Crystal Methods	12
References	13

1. ENERGY AND STRUCTURE

Table S1 summarizes a large number of previous $T = 0$ DFT calculations [1–18] obtained for a range of DFT codes and DFT parameters. These results were assembled for B19', as well as for B19" and B33 where available. A weakly stable phase (B19") has been reported recently which is a monoclinic structure very similar to B19', except with a larger monoclinic angle (around 102° instead of 98°). The existence of B19" is somewhat controversial with assertions that it may be a computational artifact. The table also reports if a non-zero shear stress was obtained for the B19' cell at a fixed monoclinic angle. While B19' is often found to be unstable, the exceptions are for calculations with small valences or where the valence was not explicitly indicated. Our calculations indicate a similar trend where including p and s electrons in the valence destabilizes B19'. We have found that when a calculation is sufficiently converged with respect to smearing value and k-point mesh, B19" is destabilized, though weakly so. At $T = 0$ K, we find only B33 to be stable with respect to phonons and cell stresses.

Table S2 shows experimental formation energies [19–22] of B2 as well as the calculated formation energies [1–3, 13, 16, 23–25] of B2, B19', B19", and B33. The present B2 formation energies are within the range of experimental uncertainty and in good agreement with the values of Hatcher, [3] which were calculated with an all-electron method. The formation energies of B19' and B33 calculated by Hatcher are 14–15 meV/atom lower in energy than the present Ni Ti_{pv} calculations.

The varied results shown in Table S1 and Table S2 clearly show that convergence criteria must be studied carefully for this material. We examined the effect on the energetic landscape caused by various calculation convergence parameters. Figures S1

and S2 show the lowest energy structures (referenced to B2) for a range of γ from 99° to 107.5° (approximately B33) with different calculation parameters. PAW potentials with different core/valence configurations are shown in Figure S1 for 16380 k-points per inverse atom and an electron smearing width of 0.05 eV. The Ni Ti potential deviates from the potentials with more valence electrons (up to 6.1 meV/atom compared to Ni_{pv} Ti_{sv}). The other potentials are all within 1.3 meV/atom of one other. The Ni Ti potential is also differentiated from the others in that it yields a stable B19" phase while the others yield no energy minima aside from B33. This result parallels the calculations shown in Table S1 where the potentials with the smaller valences produced phases that were not stable when calculated with larger valences.

In Figure S2, we show a similar set of calculations, but instead of changing the valence electrons, the k-point mesh and electron smearing parameter, sigma, are varied. We found that B19" was stable for larger smearing parameters and less dense meshes, but exploring denser meshes (up to 116,000 k-points per inverse atom) with smaller sigma values (0.01 eV) yielded no stable B19" phase. For the PBE PAW potentials included with VASP, our convergence tests show that B19' is not a T=0 K energy minima, and B19" is only a minima for the smallest valence PAW calculations. When these two phases are found with VASP PAW potentials, it is likely because of loose convergence.

In Table S3, the $T = 0$ K lattice parameters for the 4-atom unit cells of B2, B19', and B33 are shown. As B19' is not a stable minimum on the zero temperature energy profile, the shown parameters are obtained from fixing the angle to 98.0° . The zero-temperature structures have been employed [4, 5] to comment on possible transition paths between the various phases. Most notably, the large b lattice parameter of

B33, 4.923 Å, is much larger than that of the other phases. There are transition paths that include B33 as an intermediate; however, such paths would lead to large variations in b that would be unfavorable.

2. FINITE TEMPERATURE OPTIMIZATION

The free energy of the B33, B19', and B2 phases were optimized with respect to lattice parameters at temperature to produce structures having negligible stress. The optimization scheme is iterative and entails performing 3 ps DFT-MD simulations, obtaining stresses averaged over this period, and altering the cell according to $\Omega^{k+1} = \Omega^k - \alpha \frac{\partial F}{\partial \Omega}$, where Ω is a tensor describing the cell shape, F is the Helmholtz free energy, “ k ” is an iteration index, and α is a constant parameter. For a generalized crystal, Ω is given by

$$(1) \quad \Omega = \begin{bmatrix} a_x & b_x & c_x \\ a_y & b_y & c_y \\ a_z & b_z & c_z \end{bmatrix},$$

where the lattice vectors are $\mathbf{a} = (a_x, a_y, a_z)$, $\mathbf{b} = (b_x, b_y, b_z)$, and $\mathbf{c} = (c_x, c_y, c_z)$. This procedure was iterated until all components of σ were < 1 kbar, which is considered here to be stress-free and a free energy minimum.

The value of $\frac{\partial F}{\partial \Omega}$ can be written as in terms of Ω and the stress tensor, σ . The free energy of the system in the canonical ensemble is given by

$$(2) \quad F = -\beta^{-1} \ln(\mathcal{Z}),$$

where F is the Helmholtz free energy, \mathcal{Z} is the partition function, and β^{-1} is equal to the product of the Boltzmann constant and temperature. The partition function is given by $\mathcal{Z} = \int \Pi_{i=1}^N d\mathbf{r}_i d\mathbf{p}_i e^{-\beta\mathcal{H}}$, where $\int \Pi_{i=1}^N d\mathbf{r}_i d\mathbf{p}_i \dots$ represents the integral over phase space. The Hamiltonian, \mathcal{H} , describing this system is

$$(3) \quad \mathcal{H} = \sum_{i=1}^N \frac{\mathbf{p}_i \cdot \mathbf{p}_i}{2m_i} + U(\{\mathbf{r}_i\}),$$

where \mathbf{p}_i and m_i are the momentum and mass of particle “i”, the summation in the first term is taken over the N atoms in the system, and U is potential energy, which is determined by the set of all atomic positions $\{\mathbf{r}_i\}$. The derivative of F with respect to Ω is given by

$$(4) \quad \frac{\partial F}{\partial \Omega} = -\beta^{-1} \frac{1}{\mathcal{Z}} \frac{\partial \mathcal{Z}}{\partial \Omega}.$$

One may expand the derivative of \mathcal{Z} with respect to Ω by performing a canonical transformation on the coordinates \mathbf{r} and momenta \mathbf{p} , such that

$$(5) \quad \begin{aligned} \mathbf{r}_i &= \Omega \boldsymbol{\rho}_i \\ \mathbf{p}_i &= \boldsymbol{\pi}_i \Omega^{-1}, \end{aligned}$$

where $\boldsymbol{\rho}_i$ are reduced coordinates, $\boldsymbol{\pi}_i$ are transformed momentum, and a superscript “-1” indicates the inverse tensor. This transformation preserves the dynamics derived from the Hamiltonian, and leads to the partition function being written as $\int \Pi_i d\boldsymbol{\pi}_i d\boldsymbol{\rho}_i e^{-\beta\mathcal{H}(\{\boldsymbol{\pi}_i\}, \{\boldsymbol{\rho}_i\})}$. The free energy expression in Eq. 4 then reduces to

$$(6) \quad \frac{\partial F}{\partial \Omega} = \left\langle \frac{\partial \mathcal{H}(\{\boldsymbol{\pi}_i\}, \{\boldsymbol{\rho}_i\})}{\partial \Omega} \right\rangle,$$

where $\langle \dots \rangle$ denotes the ensemble average. The transformed Hamiltonian is given by

$$(7) \quad \mathcal{H} = \sum_{i=1}^N \frac{1}{2m_i} (\boldsymbol{\pi}_i \Omega^{-1}) \cdot (\boldsymbol{\pi}_i \Omega^{-1}) + U(\{\Omega \boldsymbol{\rho}_i\}).$$

The derivative of \mathcal{H} with respect to Ω may then be written as

$$(8) \quad \frac{\partial \mathcal{H}}{\partial \Omega} = \sum_{i=1}^N \frac{1}{m_i} (\boldsymbol{\pi}_i \Omega^{-1}) \cdot \frac{\partial (\boldsymbol{\pi}_i \Omega^{-1})}{\partial \Omega} + \sum_{i=1}^N \frac{\partial U}{\partial (\Omega \boldsymbol{\rho}_i)} \cdot \frac{\partial (\Omega \boldsymbol{\rho}_i)}{\partial \Omega}.$$

Employing vector-matrix manipulations, one may rearrange Eq. 8 as

$$(9) \quad \frac{\partial \mathcal{H}}{\partial \Omega} = - \sum_{i=1}^N \frac{1}{m} (\boldsymbol{\pi}_i \Omega^{-1}) \otimes (\boldsymbol{\pi}_i \Omega^{-1}) \Omega^{-T} - \sum_{i=1}^N \mathbf{f}_i \otimes \boldsymbol{\rho}_i,$$

where \mathbf{f} is force, \otimes is the outer product operation, and “ $-T$ ” indicated the transpose of the inverse. Transforming back to \mathbf{p} and \mathbf{r} leads to

$$(10) \quad \frac{\partial \mathcal{H}}{\partial \Omega} = - \sum_{i=1}^N \frac{1}{m_i} (\mathbf{p}_i \otimes \mathbf{p}_i) \Omega^{-T} - \sum_{i=1}^N (\mathbf{f}_i \otimes \mathbf{r}_i) \Omega^{-T}.$$

The quantity given by $-\sum_{i=1}^N \{\frac{1}{m} (\mathbf{p}_i \otimes \mathbf{p}_i) + (\mathbf{f}_i \otimes \mathbf{r}_i)\}$ is the product of the absolute value of the determinant of Ω^T , or volume, with the stress tensor, $|det\Omega^T|\sigma$. Using these relations with Eq. 6 leads to the final expression for the derivative of free energy,

$$(11) \quad \frac{\partial F}{\partial \Omega} = |det\Omega^T|(\sigma \Omega^{-T}),$$

which may be employed to optimize F with respect to lattice vectors.

3. PHONON DISPERSIONS

In Figure S3, the well known phonon dispersion of the cubic unit cell at $T = 0$ K of B2 is given as a function of supercell size. The smaller end of the size range,

$3 \times 3 \times 3$ to $5 \times 5 \times 5$ supercells, are given in Figure S3a. Increasing size from $3 \times 3 \times 3$ to $5 \times 5 \times 5$ reduces the frequency of the imaginary modes. Additionally, there is some minor distortion of low frequency modes in the $M \rightarrow \Gamma$ direction, near the Γ -point. The $5 \times 5 \times 5$ supercell results in imaginary frequencies near the Γ -point. To remove any ambiguity in the discussion of size effects on the B2 phonons, we have computed the phonon dispersions for $6 \times 6 \times 6$, $7 \times 7 \times 7$, and $8 \times 8 \times 8$ supercell. A comparison of the dispersions at these sizes, given in Figure S3b, indicates that size effects are effectively mitigated by using a $6 \times 6 \times 6$ or larger supercell. With respect to the smaller sizes, the anomalous imaginary modes near the Γ point vanish at these large sizes, and a fine structure of the imaginary modes along the $X \rightarrow M$ direction develops.

The $T = 0$ K phonon dispersions of the monoclinic B19', and B33 phases are given in Figures S4 and S5). As opposed to B2, the unit cell for the monoclinic phases contains 4 atoms. For these systems, phonon dispersions have been computed for $3 \times 2 \times 2$, $4 \times 3 \times 3$, and $5 \times 4 \times 4$ supercells, each of which has similar a , b , and c lattice parameters. For all of these cells, the influence of size is relatively minor, with the acoustic modes along the $\Gamma \rightarrow E \rightarrow Z$ path exhibiting variations of roughly 1 THz.

The influence of supercell on zero temperature phonon dispersions arises from interactions of images of displaced atoms. In a dynamical system, the number of existing phonon modes is a finite number that is determined by the size of the system. Simulations using larger supercells will have a denser population of phonon modes in reciprocal space. The vibrational properties resulting from such a dynamical simulation must therefore be converged with respect to supercell size.

A more explicit analysis of supercell size effects on the T -dependent vibrations is through the computation of T -dependent phonon dispersions. We show such a

dispersions for the 3x3x3 supercell of the 2 atom B2 unit cell at 300, 600, and 900 K in Figure S6. From this size, the imaginary modes centered about the M-point persist up to 600 K. At 900 K, the imaginary modes are not present, and the B2 crystal is assumed stable. The B2 phonon dispersion is also shown for a 6x6x6 supercell in Figure S7. In this case, there are no imaginary modes all the way down to 300 K, suggesting phase stability. These results are in qualitative agreement with our previous analysis of size effects in the $T = 0$, and again suggests phase stability is strongly influence by system size in the 3x3x3 unit cell.

Many of our free energy energy computations utilize the 4 atom unit cell for DFT-MD simulations. To complete our analysis of size effects, we provide the stability behavior of the 4x3x3 supercell in terms of T -dependent phonons in Figure S7. We have chosen a 4x3x3, 144 atom supercell of 4 atom unit cells for our free energy computations. As with the 6x6x6 supercell, the 4x3x3 supercell exhibits stability down to 300 K.

4. FREE ENERGY: GENERALIZED STRESS-STRAIN METHOD

A path between the low temperature monoclinic phases of NiTi, B33 and B19', and the high temperature phase, B2, can be established as a function of the monoclinic angle, γ . This presents a natural path variable for the computation of free energy. The free energy changes resulting from distortion of lattice vectors have been previously described for the limited case of the constant volume bcc \rightarrow fcc Bain path. [26] We here generalize this formalism to treat the variable volume deformation of any cell. Incorporation of variable volume allows for a transformation path between two stable phases at a given temperature but different volumes, which is the case for

NiTi phases of interest. Because the present investigation occurs at zero pressure, the resulting difference in free energy is equivalent to Gibbs free energy.

The Ω tensor can be continuously deformed from the low temperature monoclinic phases to the high temperature B2 phase. This deformation can be effected by defining Ω to be dependent on a mixing parameter, λ , that linearly changes Ω from an initial state to a final state, or $\Omega(\lambda) = \Omega^0 - \lambda(\Omega^0 - \Omega^1)$. The values of Ω at $\lambda = 0$ and 1 correspond to structures of stable phases, Ω^0 and Ω^1 , respectively. Through the use of Eq. 4, the free energy change upon such a deformation may be represented as

$$(12) \quad \Delta F = -\beta^{-1} \int_0^1 \frac{1}{Z} \frac{\partial Z}{\partial \lambda} d\lambda = -\beta^{-1} \int_0^1 \frac{1}{Z} \frac{\partial Z}{\partial \Omega} : \frac{\partial \Omega}{\partial \lambda} d\lambda,$$

where $\frac{\partial Z}{\partial \Omega}$ and $\frac{\partial \Omega}{\partial \lambda}$ are both tensors and “ $:$ ” denotes the Frobenius inner product (*i.e.*, $\sum_{ij} \frac{\partial Z}{\partial \Omega_{ij}} \frac{\partial \Omega}{\partial \lambda_{ij}}$). The changes in Helmholtz free energy given by Eq. 12 do not require a constant volume. When the integration is performed between zero-pressure states, as in the present work, the resulting measure of free energy is equivalent to Gibbs free energy. The free energy expression in Eq. 12 further reduces to

$$(13) \quad \Delta F = \int_0^1 \left\langle \frac{\partial \mathcal{H}(\boldsymbol{\pi}, \boldsymbol{\rho})}{\partial \Omega} \right\rangle : \frac{\partial \Omega}{\partial \lambda} d\lambda.$$

Using Eq. 10 with Eq. 13 leads to the final expression for free energy,

$$(14) \quad \Delta F = \int_0^1 V_\lambda \left[(\sigma \Omega^{-T}) : \frac{\partial \Omega}{\partial \lambda} \right] d\lambda,$$

where V_λ is defined as $|det \Omega^T|$.

For NiTi, the lattice vectors of both the low-temperature martensite B33 and B19' structures as well as the high-temperature B2 structure can be represented as

a tensor Ω , given by

$$(15) \quad \Omega = \begin{bmatrix} a_x & b_x & 0 \\ 0 & b_y & 0 \\ 0 & 0 & c_z \end{bmatrix}.$$

Using this with Eq. 11 leads to

$$(16) \quad \Delta F = \int_0^1 V_\lambda \left\{ \sigma_{xx} \frac{\partial \ln a_x}{\partial \lambda} + \sigma_{yy} \frac{\partial \ln b_y}{\partial \lambda} + \sigma_{zz} \frac{\partial \ln c_z}{\partial \lambda} - \sigma_{xy} \frac{b_x}{b_y} \left[\frac{\partial \ln a_x}{\partial \lambda} - \frac{\partial \ln b_x}{\partial \lambda} \right] \right\} d\lambda.$$

The stresses in this formulation are obtained from DFT-MD simulations, which must be suitably long to provide a well-converged measure of stress. The time averages of stress components required for Eq. 16 are given in Figure S8. Stresses are given for the B2 ($\lambda = 0$) and B19' ($\lambda = 1$) phases, as well as for an interpolated structure between these phases ($\lambda = 0.5$). In all cases, the stresses converge in a well-behaved manner and reach full convergence, which is defined to be within 1 kbar of the long-time average, within a few picoseconds. As a standard practice in the present work, we employ 10 ps DFT-MD simulations for points along our stress strain λ path.

The numerical accuracy of the DFT techniques could influence the average stress obtained from MD simulations, as well as the resulting measure of free energy. Free energy profiles along λ for various levels of numerical accuracy are presented in Figure S9. For each numerical configuration, the structure of B2 and B19', which correspond to λ values of 0 and 1, respectively, have been fully optimized. DFT-MD simulations are performed for nine structures (a λ spacing of 0.1) obtained by linearly interpolating between B2 and B19', B2 - λ (B2 - B19'). Our default simulation parameters correspond to the Ni Ti_{pv} pseudo potential, a 6x5x6 k-point mesh, a 269.5 eV

energy cutoff, and a energetic convergence criteria of 10^{-7} . To evaluate the tolerance of free energy to these parameters, we have performed single substitutions of each parameter and recomputed the free energy profile. Employing the large Ni Ti core results in variations along the λ path but no significant change in $F(1) - F(0)$. For k-points, both 4x4x4 and 7x7x7 k-point meshes have been employed. Both meshes result in slightly higher transition barriers, though the difference between B19' and B2 free energies agrees with that obtained from simulations with the default parameters. For the energy cutoff. As with the other parameters, the energy cutoff, too, results in the same free energy differences between the stable phases as the default parameters. The free energy difference is a weak function of the above parameters. More accurate methods, including smaller cores and more accurate functionals, are not tenable to DFT-MD simulations, but could very well have a marked influence on free energy.

As a final note, the free energy profile for the generalized stress-strain method represents a single interpolated path between two phases in lattice vector configuration space. This implies that the free energy barriers are likely upper bounds to an alternative path exhibiting lower stress. Nevertheless, the path chosen for the present work coincides with motion along the [100](011) generalized stacking fault, which is meaningful as it has been experimentally conjectured as a possible physical path for transition. The changes in atomic configuration along this path are well-behaved and reversible and the resulting free energy agrees well with Einstein crystal approaches, as described in the next section. The above evidence suggests that errors resulting from loss of lattice stability along the path or from constrained cell effects [27, 28] are minimal.

5. FREE ENERGY: EINSTEIN CRYSTAL METHODS

One may additionally use the principles of thermodynamic integration.

$$(17) \quad \Delta F = \int_0^1 \left\langle \frac{\partial U}{\partial \lambda} \right\rangle_{\lambda=\lambda'} d\lambda'$$

The potential energy is taken from a reference system, which preferably has a known value of free energy, to the system of interest, given as $U = U^{ref} - \lambda(U^{ref} - U^{full})$. Choices for U^{ref} have ranged from single harmonic wells to full force constant matrix to represent the internal energy of the crystal. The spring constant is a generally poor choice for U^{ref} , while the force constant matrix is sensible if the crystal is stable and phonons are real. There are a few classes of systems where application can vary: disordered systems, ordered crystal with unstable phonons, and ordered crystals with stable phonons.

In essence, the choice of reference potential will vary with respect to system type. For the first case of a highly disordered solid system, the spring constant approach may be a sensible reference potential. For ordered crystalline systems, phonons are an excellent choice for reference potential. For ordered systems with unstable modes at $T = 0$ K, the stabilized T-dependent phonons are used as a reference potential. The convergence of U with respect to λ for all phases at 300 K is given in Figure S10. For all phases, the derivatives are shown to converge within 10 ps. Profiles of $\frac{\partial U}{\partial \lambda}$ as a function of λ are shown in Figure S11. The highly harmonic nature of B33 and B19' are exhibited in the minor variation in $\frac{\partial U}{\partial \lambda}$ over the λ range. The large variation of $\frac{\partial U}{\partial \lambda}$ for B2 may be attributed to its highly anharmonic character.

REFERENCES

- [1] J. E. Saal, S. Kirkland, M. Aykol, B. Meredig, and C. Wolverton. Materials design and discovery with high-throughput density functional theory: The open quantum materials database (OQMD). *JOM*, 65:1501–1509, 2013.
- [2] A. Jain and *et al.* Commentary: The materials project: A materials genome approach to accelerating materials innovation. *APL Mater.*, 1:011002, 2013.
- [3] M. Armand, F. Endres, D. R. MacFarlane, H. Ohno, and B. Scrosati. Electronic and phononic origins of martensitic behavior in nickel titanium-based binary and ternary shape memory alloys. *Ph.D. Thesis*, 2010.
- [4] N. Hatcher, O. Yu. Kontsevoi, and A. J. Freeman. Martensitic transformation path in NiTi. *Phys. Rev. B*, 79:020202, 2009.
- [5] N. Hatcher, O. Yu. Kontsevoi, and A. J. Freeman. Role of elastic and shear stabilities in the martensitic transformation path of NiTi. *Phys. Rev. B*, 80:144203, 2009.
- [6] G. Vishnu and A. Stachan. Size effects in NiTi from density functional theory calculations. *Phys. Rev. B*, 85:014114, 2012.
- [7] M. F.-X. Wagner and W. Windl. Lattice stability, elastic constants and macroscopic moduli of NiTi martensites from first principles. *Acta Mater.*, 56:6232–6245, 2008.
- [8] J. Wang and H. Sehitoglu. Resolving quandaries surrounding NiTi. *Appl. Phys. Lett.*, 101:081907, 2012.
- [9] X. Huang, C. Bungaro, V. Godlevsky, and K. M. Rabe. Lattice instabilities of cubic NiTi from first principles. *Phys. Rev. B*, 65:014108, 2001.
- [10] D. Holec, M. Friák, A. Dlouhý, and J. Neugebauer. *Ab initio* study of pressure stabilized NiTi allotropes: Pressure-induced transformations and hysteresis loops. *Phys. Rev. B*, 84:224119, 2011.
- [11] S. Kibey, H. Sehitoglu, and D.D. Johnson. Energy landscape for martensitic phase transformation in shape memory NiTi. *Acta Mater.*, 57:1624–1629, 2009.
- [12] P. Šesták, M. Černý, and J. Pokluda. On the effect of deformation twins on stability of B19' structure in NiTi martensite. *Comput. Mater. Sci.*, 87:107–111, 2014.

- [13] A. Pasturel, C. Colinet, D.N. Manh, A.T. Paxton, and M. van Schilfgaarde. Electronic structure and phase stability study in the Ni-Ti system. *Phys. Rev. B*, 52:15176–15190, 1995.
- [14] K. Parlinski and M. Parlinska-Wojtan. Lattice dynamics of NiTi austenite, martensite, and R phase. *Phys. Rev. B*, 66:064307, 2002.
- [15] X.-Q. Wang. Twinned structure for shape memory: First-principles calculations. *Phys. Rev. B*, 78:092103, 2008.
- [16] Y.Y. Ye, C.T. Chan, and K.M. Ho. Structural and electronic properties of the martensitic alloys TiNi, TiPd, and TiPt. *Phys. Rev. B*, 56:3678–3689, 1997.
- [17] Z.-Y. Zeng, C.-E. Hu, L.-C. Cai, X.-R. Chen, and F.-Q. Jing. Molecular dynamics study of the melting curve of NiTi alloy under pressure. *J. Appl. Phys.*, 109:043503, 2011.
- [18] D. Mutter and P. Nielaba. Simulation of structural phase transitions in NiTi. *Phys. Rev. B*, 82:224201, 2010.
- [19] R. Hu, P. Nash, and Q. Chen. Enthalpy and formation of the Al-Ni-Ti system. *J. Phase Equilibria Diffus.*, 30:559–563, 2009.
- [20] O. Kubaschewski. The heats of formation in the system aluminum + nickel + titanium. *Trans. Faraday Soc. Engl.*, 54:814–820, 1958.
- [21] J.C. Gachon, M. Notin, and J. Hertz. The enthalpy of mixing of the intermediate phases in the systems FeTi, CoTi, and NiTi by direct reaction calorimetry. *Thermochim. Acta*, 48:155–164, 1981.
- [22] Q. Guo and O.J. Kleppa. Standard enthalpies of formation of some alloys formed between group iv elements and group viii elements, determined by high-temperature direct synthesis calorimetry: II. alloys of (Ti, Zr, Hf) with (Co, Ni). *J. Alloys Compd.*, 269:181–186, 1998.
- [23] J. Lu, Q. Hu, and R. Yang. A comparative study of elastic constants of NiTi and NiAl alloys from first-principle calculations. *J. Mater. Sci. Technol.*, 25:215–218, 2009.
- [24] J.E. Douglas and *et al.* Phase stability and property evolution of biphasic Ti-Ni-Sn alloys for use in thermoelectric applications. *J. Appl. Phys.*, 115:043720, 2014.

- [25] T. Tokunaga, K. Hashima, H. Ohtani, and M. Hasebe. Thermodynamic analysis of the Ni-Si-Ti system using thermochemical properties determined from *Ab Initio* calculations. *Mater. Trans.*, 45:1507–1514, 2004.
- [26] C. Carzola, D. Alf  , and M. J. Gillan. Constraints on the phase diagram of molybdenum from first-principles free-energy calculations. *Phys. Rev. B*, 85:064113, 2012.
- [27] V. Ozolins. First-principles calculations of free energies of unstable phases: the case of fcc w. *Phys. Rev. Lett.*, 102:065702, 2009.
- [28] A. van de Walle, Q. Hong, S. Kadkhodaei, and R. Sun. The free energy of mechanically unstable phases. *Nat. Commun.*, 6:7559, 2015.

TABLE S1. Survey of literature results for the relative energies of B19', B19" and B33 with respect to B2 for different DFT codes and DFT parameters.

	Program	Method	XC	Valence	Spin	E-E ^{B2} (meV/atom)			
						B19'	Stable?	B19"	B33
OQMD [1]	VASP	PAW	PBE	Ni Ti	yes	-31.0	yes(98.3)		
Materials Project [2]	VASP	PAW	PBE	Ni _{pv} Ti _{pv}	yes			-54.2	
Hatcher [3–5]		FLAPW	PBE	All electron	no	-56.0	no		-60.1
Vishnu [6]	SeqQuest	LCAO NC PP	PBE	Ni Ti _{pv}	no	-40.5	no	-43.5	-46.0
Vishnu [6]	SeqQuest	LCAO NC PP	PBE	Ni Ti	no	-40.5	yes	-46.5	-48.5
Wagner [7]	VASP	PAW	PW91	Ni Ti _{pv}	yes	-44.0	no		-49.5
J. Wang [8]	VASP	PAW	PW91		no	-44.1	yes	-51.4	-52.4
Huang [9]	VASP	USPP	LDA	Ni Ti _{pv}	yes	-49.0	no		-54.0
Huang [9]	VASP	PAW	LDA	Ni Ti _{pv}	yes			-54.0	
Huang [9]	VASP	USPP	PW91	Ni Ti _{pv}	yes	-42.0	no		-50.0
Holec [10]	VASP	PAW	PBE		no	-33.5	yes(95.3)	-41.5	-42.0
Kibey [11]	VASP	PAW	PW91		no	-39.5	yes		
Sestak [12]	VASP	PAW	PW91	Ni Ti _{pv}	no	-40.3	no		-48.0
Sestak [12]	ABINIT	NC PP	PBE	Ni Ti	no	-13.6	no		-66.4
Pasturel [13]		LMTO-ASA	LDA	All electron	no	-17.6	yes (96.8)		
Pasturel [13]		FP-LMTO	LDA	All electron	no	-18.7	yes (96.8)		
Parlinski [14]	VASP	USPP	GGA	Ni Ti	no	-43.0	yes		
X. Wang [15]	VASP	PP	LDA		no	-51.0	yes		
Ye [16]		NC PP	LDA		no	-45.0	yes		
Zeng [17]	VASP	PAW	PBE	Ni _{pv} Ti _{pv}	no	-42.9	yes		-44.7
This work	VASP	PAW	PBE	Ni Ti	yes	-39.6	no	-41.2	-41.6
This work	VASP	PAW	PBE	Ni Ti _{pv}	yes	-38.2	no		-41.5
This work	VASP	PAW	PBE	Ni _{pv} Ti _{pv}	yes	-40.6	no		-44.2
This work	VASP	PAW	PBE	Ni Ti _{sv}	yes	-38.4	no		-41.7
This work	VASP	PAW	PBE	Ni _{pv} Ti _{sv}	yes	-40.8	no		-44.5
Mutter [18]		EAM				-54.0	yes		

LCAO: Linear Combination of Atomic Orbitals

Ni: 3d9 4s1

NC: Norm Conserving

Ni_{pv}: 3p6 3d8 4s2

PP: Pseudopotentials

Ti: 3d3 4s1

PAW: Projector Augmented Waves

Ti_{pv}: 3p6 3d3 4s1

EAM: Embedded Atom Method

Ti_{sv}: 3s2 3p6 3d3 4s1

FLAPW: Full Potential Linearized Augmented Plane Wave Method

USPP: Ultrasoft Pseudopotential

LMTO-ASA: Linear Muffin Tin Orbital-Atomic Sphere Approximation

FP-LMTO: Full Potential-Linear Muffin Tin Orbital

TABLE S2. Formation energies of NiTi phases.

Experimental Method		E ^{form} (eV/atom)									
		B2	B19'	Stable?	B19"	B33					
Hu [19]	Direct reaction calorimetry				-0.3742						
Kubaschewski [20]	Direct reaction calorimetry				-0.3513						
Gachon [21]	Direct reaction calorimetry				-0.3524						
Guo [22]	Direct reaction calorimetry				-0.3431						
		Program	DFT Method	XC	Valence	Spin	B2	B19'	Stable?	B19"	B33
OQMD [1]	VASP	PAW	PBE	Ni Ti	yes	-0.378	-0.409	yes(98.3)			
Materials Project [2]	VASP	PAW	PBE	Ni _{pv} Ti _{pv}	yes	-0.3437				-0.3979	
Hatcher [3–5]		FLAPW	PBE	All electron	no	-0.353	-0.409	no			-0.4135
Pasturel [13]		LMTO-ASA	LDA	All electron	no	-0.3949	-0.4125	yes (96.8)			
Pasturel [13]		FP-LMTO	LDA	All electron	no	-0.3731	-0.3918	yes (96.8)			
Lu [23]		EMTO-CPA	PBE	Ni Ti	no	-0.34					
Douglas [24]	VASP	PAW	PBE		yes	-0.411					
Tokunaga [25]		FLAPW	GGA	All electron	no	-0.3585					
Ye [16]		NC PP	LDA		no	-0.66	-0.705	yes			
This work	VASP	PAW	PBE	Ni Ti	yes	-0.3439	-0.3835	no		-0.3851	-0.3855
This work	VASP	PAW	PBE	Ni Ti _{pv}	yes	-0.3574	-0.3955				-0.3989
This work	VASP	PAW	PBE	Ni _{pv} Ti _{pv}	yes	-0.3555	-0.3961	no			-0.3997
This work	VASP	PAW	PBE	Ni Ti _{sv}	yes	-0.3574	-0.3958	no			-0.3991
This work	VASP	PAW	PBE	Ni _{pv} Ti _{sv}	yes	-0.3557	-0.3965	no			-0.4002

PAW: Projector Augmented Waves

Ni: 3d9 4s1

FLAPW: Full Potential Linearized Augmented Plane Wave Method

Ni_{pv}: 3p6 3d8 4s2

LMTO-ASA: Linear Muffin Tin Orbital-Atomic Sphere Approximation

Ti: 3d3 4s1

FP-LMTO: Full Potential-Linear Muffin Tin Orbital

Ti_{pv}: 3p6 3d3 4s1

EMTO-CPA: Exact Muffin Tin Orbitals-Coherent Potential Approximation

Ti_{sv}: 3s2 3p6 3d3 4s1

PAW: Projector Augmented Waves

NC PP: Norm Conserving Pseudopotentials

TABLE S3. Structure of $T = 0$ K phases of NiTi.

Phase	Group	a	b	c	γ	V
B2	$Pm\bar{3}m$	3.007	4.260	4.260	90.00	13.67
B19'	$P2_1/m$	2.922	4.676	4.058	98.00†	13.72
B33	$Cmcm$	2.925	4.923	4.015	107.32	13.80

†angle fixed

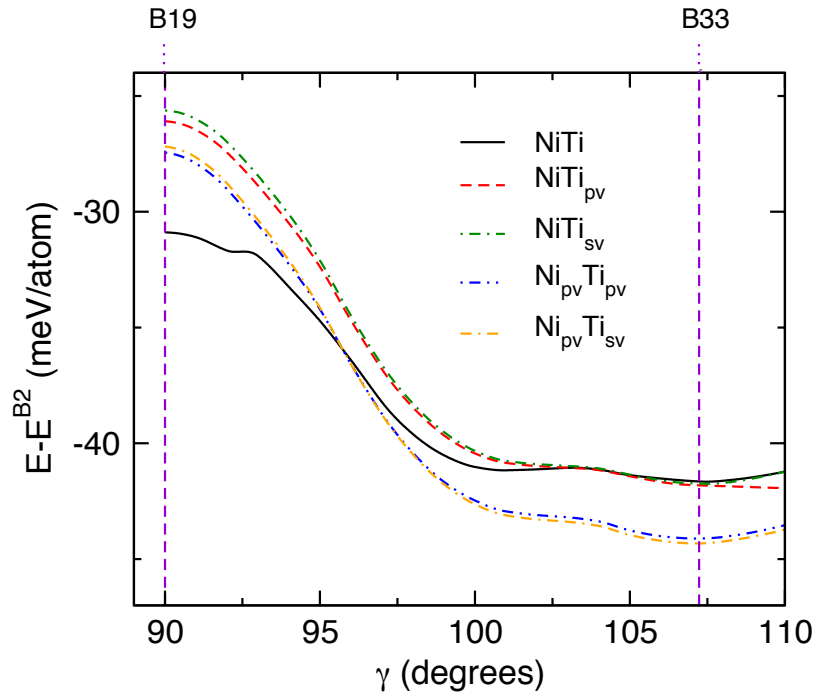


FIGURE S1. Energy of NiTi versus monoclinic angle, γ , for different pseudopotential core size.

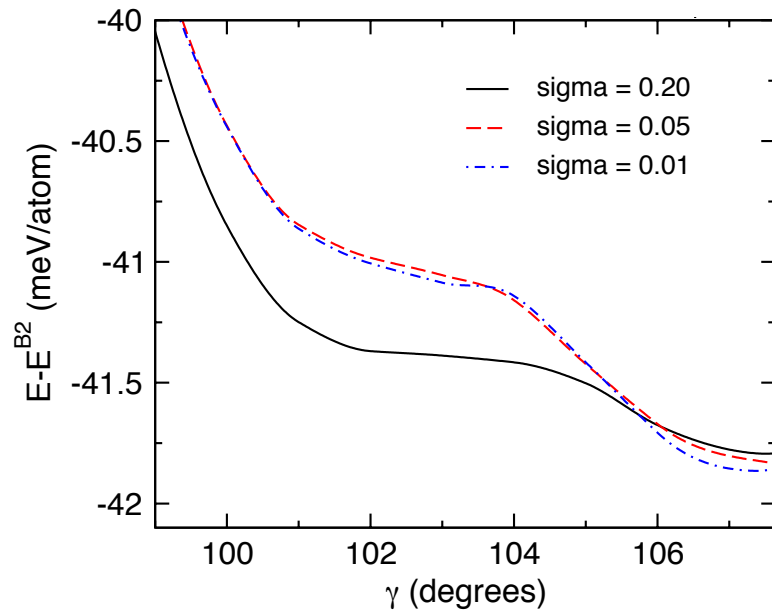


FIGURE S2. Energy of NiTi versus monoclinic angle, γ , for different electron smearing width, sigma.

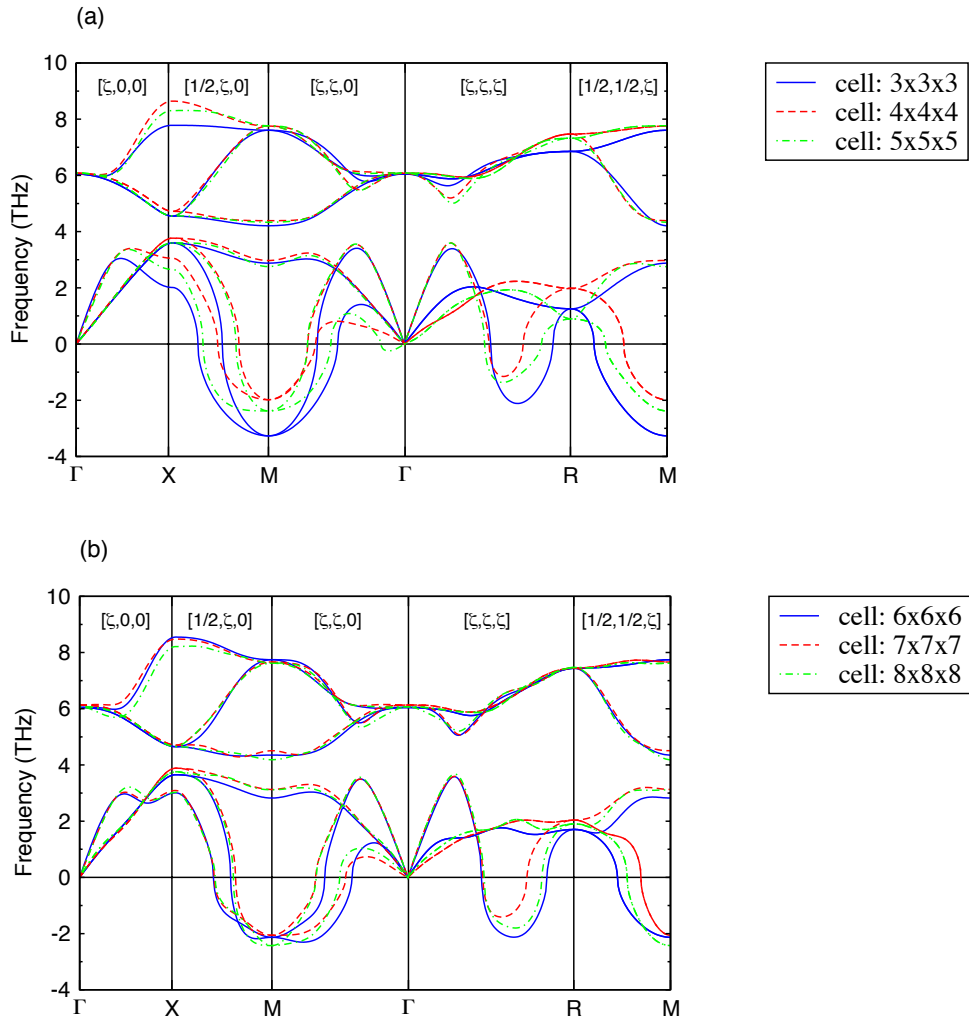


FIGURE S3. Phonon dispersion of cubic B2 NiTi for 3x3x3 to 8x8x8 supercells.

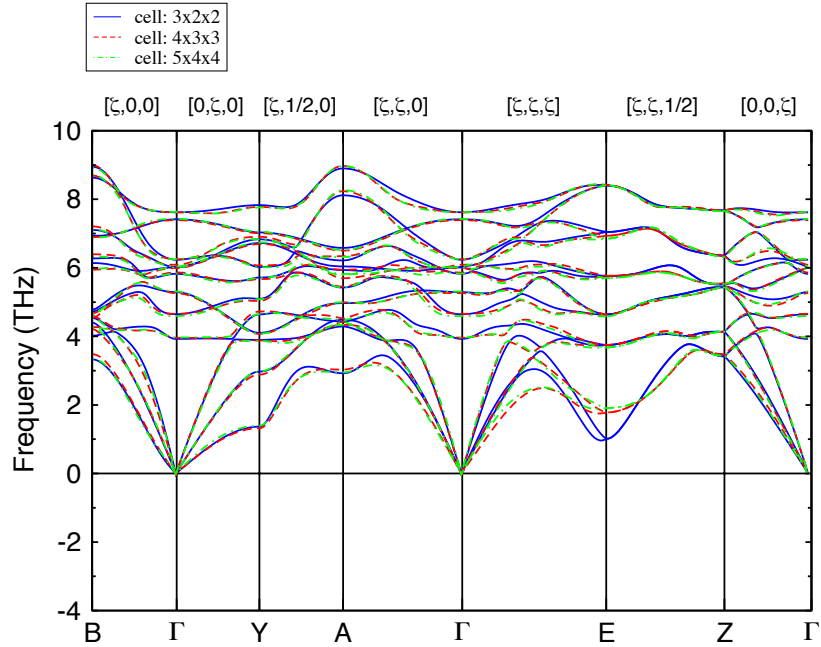


FIGURE S4. Phonon dispersion of B19' NiTi for 3x2x2, 4x3x3, 5x4x4 supercells.

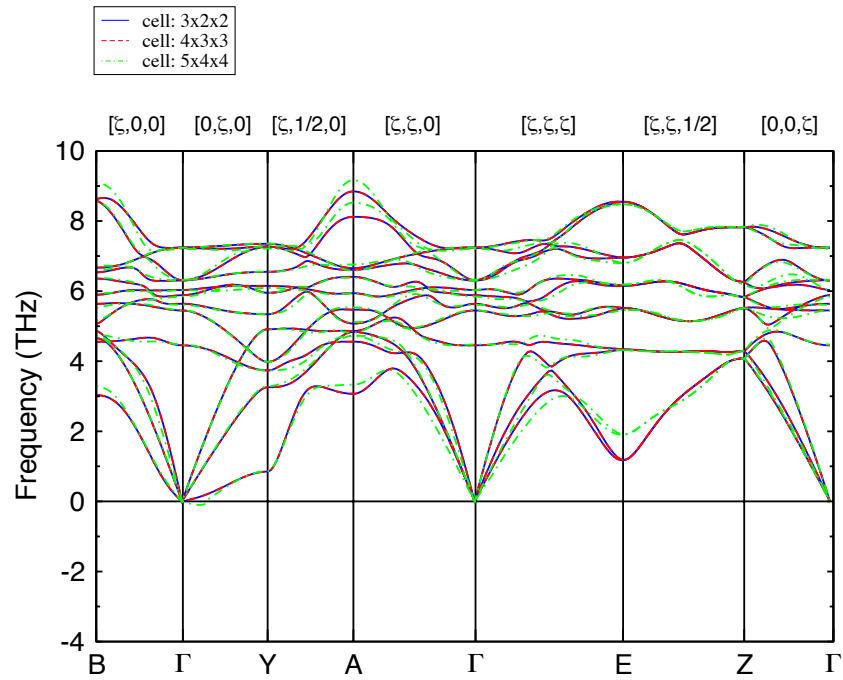


FIGURE S5. Phonon dispersion of B33 NiTi for 3x2x2, 4x3x3, 5x4x4 supercells.

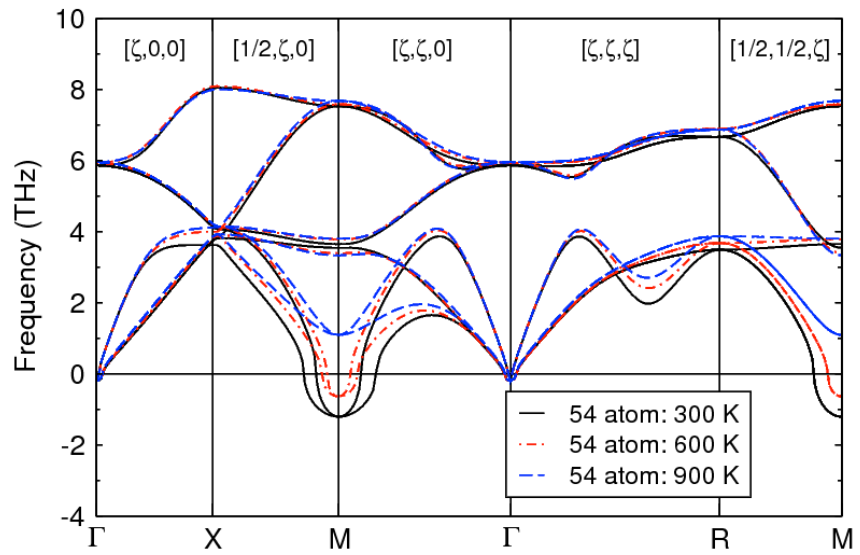


FIGURE S6. Phonon dispersion of a 3x3x3 supercell of B2 NiTi at 300, 600 and 900 K.

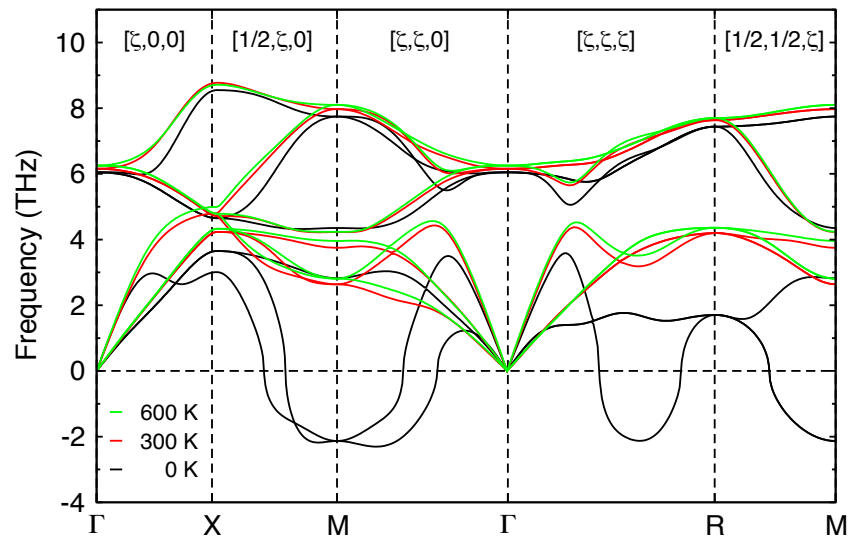


FIGURE S7. Phonon dispersion of a 6x6x6 supercell of B2 NiTi at 0, 300, and 600 K.

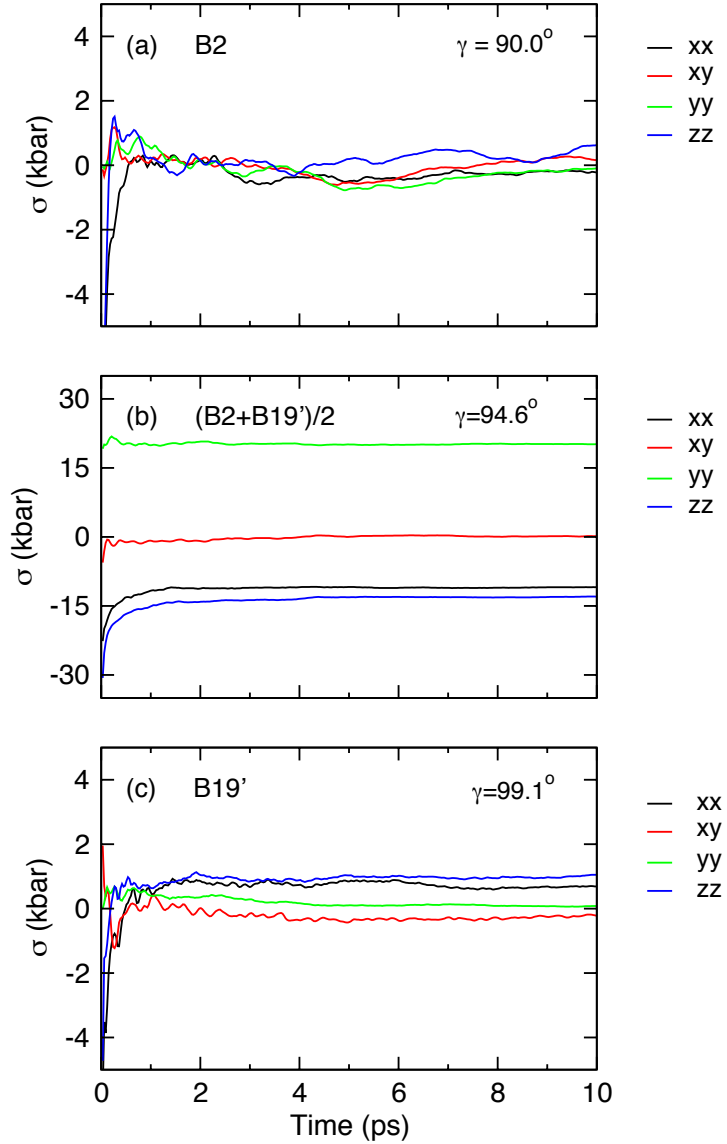


FIGURE S8. Convergence of (a) B2, (b) the interpolated structure half-way between B2 and B19', and (c) B19' stress components employed for free energy with respect to simulation time at 300 K for 4x3x3 supercells.

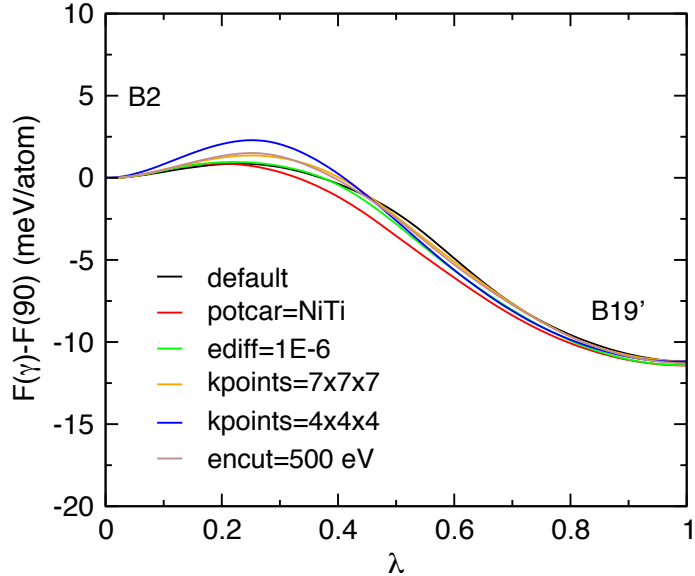


FIGURE S9. Free energy as a function of γ between B2 and B19' as determined by the stress-strain method for various levels of numerical accuracy. Results are shown for a 3x2x2 supercell having 48 atoms at 300 K. The VASP specific term potcar, ediff, and encut refer to the employed pseudopotential, the electronic energy convergence criteria, and the cutoff energy for the plane wave basis set.

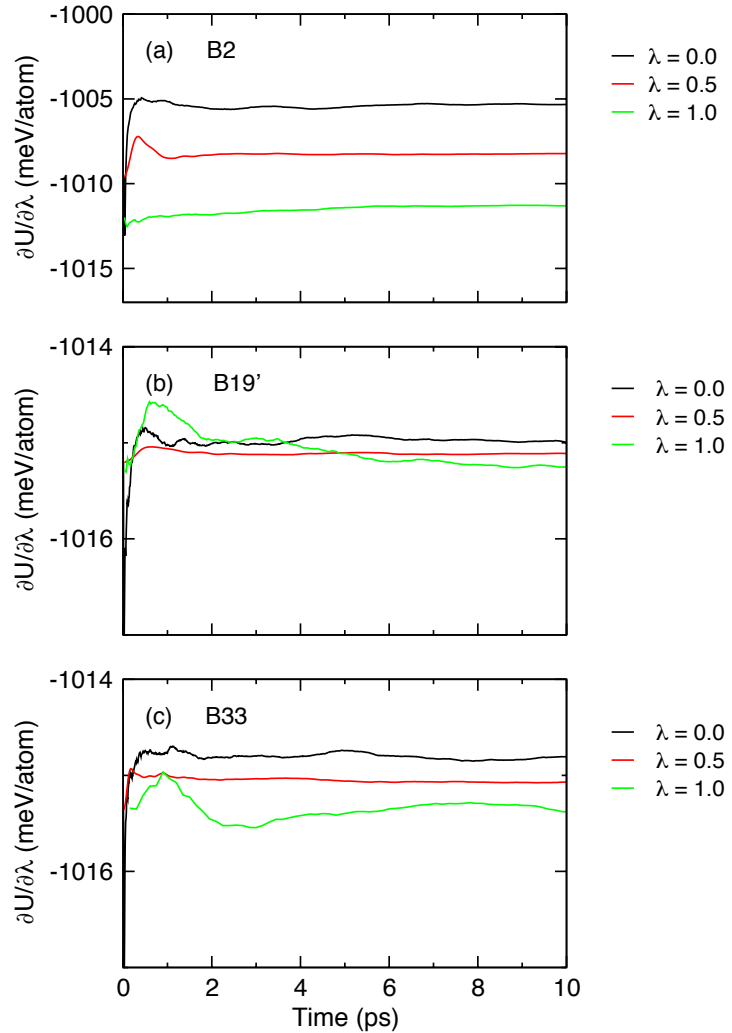


FIGURE S10. Convergence of $\langle \partial U / \partial \lambda \rangle$ at 300 K as a function of simulation time of (a) B2, (b) B19', and (c) B33. The derivative is given for constant λ values of 0.0, 0.5, and 1.0.

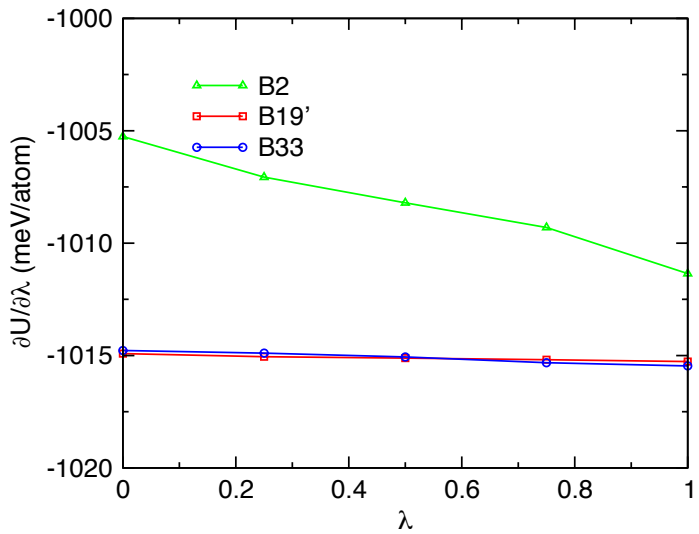


FIGURE S11. Profile of $\langle \partial U / \partial \lambda \rangle$ at 300 K as a function of λ for B2, B19', and B33. Results are shown for 300 K and a 4x3x3, 144 atom supercell.